CPP

REPRINT

Two-Temperature Warm Dense Matter Produced by Ultrashort Extreme Vacuum Ultraviolet-Free Electron Laser (EUV-FEL) Pulse

N. A. Inogamov[*1], **A. Ya. Faenov**[2,3,7], **V. V. Zhakhovsky**[2,4], **T. A. Pikuz**[2,3,7], **I. Yu. Skobelev**[2], **Yu. V. Petrov**[1], **V. A. Khokhlov**[1], **V. V. Shepelev**[5], **S. I. Anisimov**[1], **V. E. Fortov**[2], **Y. Fukuda**[3,7], **M. Kando**[3], **T. Kawachi**[3], **M. Nagasono**[7], **H. Ohashi**[7,8], **M. Yabashi**[7,8], **K. Tono**[7], **Y. Senda**[8], **T. Togashi**[7,8], and **T. Ishikawa**[7]

[1] Landau Institute for Theoretical Physics, Russian Academy of Sciences, Chernogolovka 142432, Russia

[2] Joint Institute for High Temperatures, Russian Academy of Sciences, Moscow 125412, Russia

[3] Kansai Photon Science Institute, Japan Atomic Energy Agency, Kyoto 619-0215, Japan

[4] Department of Physics, University of South Florida, Tampa, Florida 33620, USA

[5] Institute for Computer Aided Design, Russian Academy of Sciences, Moscow, 123056, Russia

[7] XFEL RIKEN, SPring-8, Hyogo 679-5198, Japan

[8] Japan Synchrotron Radiation Research Institute, SPring-8, Hyogo 679-5198, Japan

Ultrashort X-ray laser pulse acts onto electron subsystem of dielectrics such as LiF and transfers matter into a two-temperature state with hot electrons excited by the pulse from valence to conduction band. Because of the small heat conduction, the hydrodynamic motion proceeds in adiabatic regime keeping the radiation attenuation depth D_{att} as the only scale of the spatial heat distribution. Hydrodynamic motion qualitatively changes with absorbed energy increase. At low fluences $F \sim 10 \text{mJ/cm}^2$ a spallative removal of LiF remaining in solid state takes place. This is a reason for the low ablation threshold. The paper presents new experimental findings supporting this conclusion. For the first time these findings are obtained using ultrashort extreme vacuum ultraviolet-free electron laser (EUV-FEL). In the case of high fluence, also achieved in our experiments at EUV-FEL, material removal happens as result of outflow of matter transferred into the gaseous state. This explains the slow growth of the amount of ablated mass with significant fluence increase.

1 Introduction

Two-temperature warm dense matter, created by the action of the collision Ag-plasma X-ray laser (XRL) onto the lithium fluoride (LiF) crystal, has been considered in papers [1,2]. Experimental investigations have been done at Kansai Photon Science Institute (KPSI) of Japan Atomic Energy Agency (JAEA). These experiments exhibited a low threshold value of laser irradiation fluence for the onset of ablation. This low value of ablation threshold demonstrates a high efficiency of short pulse XRL in comparison with nanosecond XRL or in comparison with fs and ns optical lasers. The duration τ_L of ultrashort laser pulse is shorter than, or comparable with the acoustic time $t_s = D_{att}/c_s$ which is necessary for sound to travel with speed c_s through an attenuation depth D_{att}. Such pulses create thermo-mechanical stresses which are the reason for spallative ablation. Thermo-mechanics and negative pressure define the character of ablation at relatively low fluencies of the order of ablation threshold. At such fluencies heating is moderate and matter remains in condensed state where cohesive properties are dynamically important. At higher fluencies XRL transfers the heated layer with thickness D_{att} into gaseous state where cohesion is not significant.

* Corresponding author: E-mail: nailinogamov@googlemail.com, Phone: +07 495 425 8767, Fax: +07 495 702 9317

In dielectrics, as well as in metals, a laser pulse is absorbed by electronic subsystem of condensed matter. For short pulses, the electron-ion energy exchange time t_{eq} exceeds pulse duration τ_L and the situation with different electron temperature T_e and lattice temperature T_i ($T_e \gg T_i$) appears.

The thermodynamical state of the heated surface layer, with thickness D_{att} at fluencies under consideration, lies between the triple and critical points. Density during heating is of the order of solid state density and internal energy per atom is in the few eV range, the so called warm dense matter (WDM) range. The short pulse XRL transfers matter first into two-temperature WDM state. The two-temperature stage is an important part of the whole process.

There is a qualitative difference between the two-temperature dielectrics and metals. In metals, conduction electrons are initially present, while in dielectrics they appear as the result of photo and impact ionization from valence band. The ionization degree $Z = n_e/n_p$ is in the 1-100% range for wide-gap dielectric LiF in our range of energies, from fluencies near ablation threshold $F_{abl} \approx 10$ mJ/cm^2 and up to fluencies $F \sim 20F_{abl}$ (here n_e, n_p are free electron and LiF pairs number density respectively, $n_p = 6 \cdot 10^{22}$ cm^{-3} at room temperature). A difficult and important problem concerning value of an electron-ion energy exchange rate $\dot{E}_{ei} = \alpha(T_e - T_i)$ for dielectrics is solved in this paper. The coefficient α has remained unknown for dielectrics. Our calculations show that $\alpha \to 0$ when $Z \to 0$ and that α_{LiF} is 1.7-2 times higher than α_{Al} for aluminum at typical ionization degrees $Z \sim 0.1 - 1$ of LiF.

2 EUV-FEL experiments with LIF target

The experiment with the self-amplified spontaneous emission-free electron laser (SASE-FEL) facility was performed at the SPring-8 Compact SASE Source (SCSS). This system can provide laser pulses in the extreme-ultraviolet (EUV) region (51-62 nm) [3–5]. In our experiments, SCSS worked at wavelengths about 61.5 nm. A single shot mode was used, allowed to measure the laser energy in each shot [5]. SCSS pulse energy was varied from 4 to 11 μJ in different shots. The duration of the pulse was about 300 fs [4]. To find the ablation threshold of LiF crystals, we varied EUV-FEL energy and/or changed beam focusing position from the best focus at the surface of a LiF crystal to defocusing from the best focus up to 40 mm.

The luminescence of stable color centers (CCs) [6–8] formed by EUV-FEL radiation was used to measure the intensity/fluence distribution in SCSS laser focal spots [9]. This is very important as it allows us to define an accurate value of the real local fluence at a target surface, and to find exact values of the ablation threshold. This is significant since, due to strong abberations, the intensity distribution has complicated smeared-out shape and at near threshold F_{abl}, only a small part (20-40%) of pulse energy is inside the ablation crater.
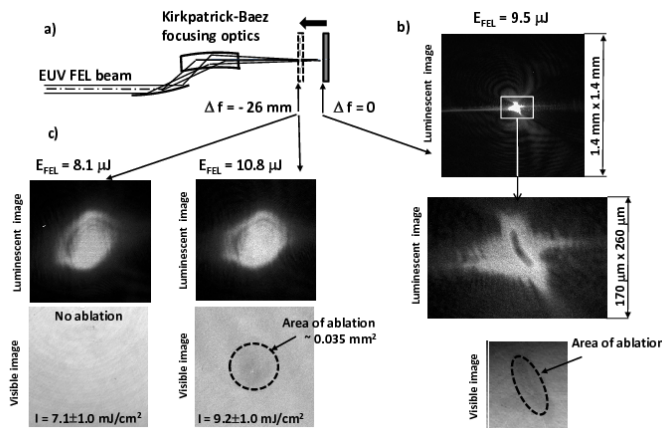

Fig. 1 a) The experimental setup for recording the 61.5 nm SCSS free electron laser beam patterns near the best focusing position on a LiF crystal. b, c) The patterns recorded on LiF crystal, placed in the best focusing position and 26 mm out of it, imaged by Olympus microscope working in luminescent and visible modes. Area of ablation is marked on the visible images.

The photo-luminescence patterns from the color centers (CCs) in LiF (after irradiation of the LiF crystal with the EUV-FEL beam) were observed by using a confocal fluorescence laser microscope (OLYMPUS model FV300). To confirm that the surface of the crystal has been damaged, we used an OLYMPUS BX60 microscope in visible and differential modes. Also, cross sections of the ablated craters were measured with an atomic force microscope (AFM, TOPOMETRIX Explorer) operating in the tapping mode. Typical images of the SCSS-FEL beam, recorded with the LiF crystal at different focusing positions, are presented in Figures 1b and 1c.

Our experiments were performed using 61.5 nm SCSS free electron laser facility. These new experimental results confirmed the low value of the ablation threshold $F_{abl} \approx 10$mJ/cm^2. From Figure 1c we can see that fluence ~ 7.1mJ/cm^2 was not sufficient for EUV-FEL production of ablation on the surface of LiF crystal. Meanwhile, fluence ~ 9.2mJ/cm^2 was sufficient to produce clear spot on the surface of the LiF crystal.
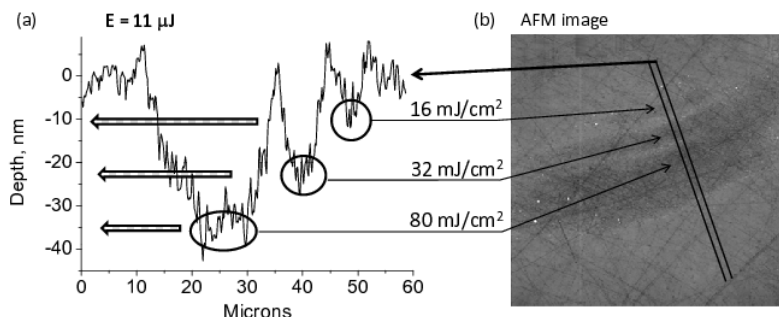

Fig. 2 a, b) Trace and AFM image of patterns recorded on LiF crystal placed 5 mm from the best focusing position. Crystal was illuminated by EUV-FEL beam with energy 11 μJ. Trace shows that different ablation zones could be selected, which corresponds to laser fluences from 16 to 80 mJ/cm^2. A low change of ablation depth from ≈ 10nm to ≈ 30nm with significant increasing of laser fluence has been observed.
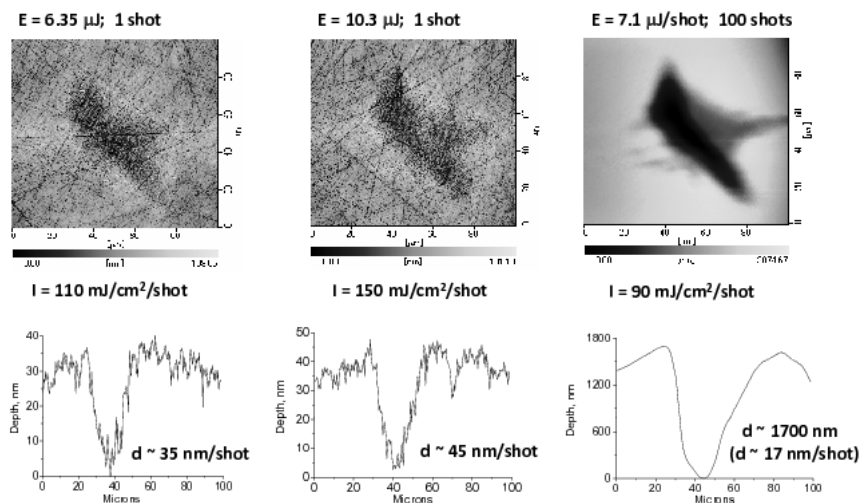

Fig. 3 AFM images and traces of patterns recorded on LiF crystal placed at the best focusing position. Crystal was illuminated by 1 and 100 shots of FEL beam with different energy. Traces of presented images clearly demonstrate that LiF crystal ablation depth increases very slowly with increasing of laser fluence and number of shots.

It is also very interesting to compare the changes of ablation depth in different ablation zones, which were irradiated by EUV-FEL with different fluencies. We have determined that the smallest depth, which appears near ablation threshold of LiF crystal, is 10-15 nm (see Fig. 2). Meanwhile, increasing laser fluence up to 80 mJ/cm^2 does not efficiently increase the ablation depth, which reaches the value of only about 30-35 nm. This result is different enough in comparison with irradiation of LiF crystals by 7 ps Ag XRL laser, where we observed the depths of ablation about 40-50 nm near the ablation threshold [1, 2]. Fig. 3 presents the results obtained by irradiation of LiF crystals at even greater intensities, proving the slow increase of ablation depth with increasing of EUV-FEL fluence. From Fig. 3 it is clear that even under irradiation of EUV-FEL fluences, about 110-150 mJ/cm^2, the ablation depth is quite small and varied at around 30-40 nm.

3 Physical model

When EUV or XRL laser pulse interacts with dielectrics, we use the next system of equations for target material parameters

$$n_p \frac{\partial Z}{\partial t} = \frac{I}{\hbar\omega_L\, D_{att}} + \nu_{imp} n_e - \kappa_{rec} n_e^3, \tag{1}$$

$$\rho^0 \frac{\partial(E_e/\rho)}{\partial t} = \frac{\rho^0}{\rho} \frac{I}{D_{att}} - n_p^0 \Delta \frac{\partial Z}{\partial t} - \frac{\rho^0}{\rho}\alpha(T_e - T_i) - p_e \frac{\partial u}{\partial x^0}, \tag{2}$$

$$\rho^0 \frac{\partial(E_i/\rho)}{\partial t} = \frac{\rho^0}{\rho}\alpha(T_e - T_i) - p_i \frac{\partial u}{\partial x^0}, \tag{3}$$

$$\rho^0 \frac{\partial u}{\partial t} = -\frac{\partial p}{\partial x^0}, \tag{4}$$

$$\rho(x^0, t)\frac{\partial x(x^0, t)}{\partial x^0} = \rho^0, \tag{5}$$

$$\frac{\partial x(x^0, t)}{\partial t} = u(x^0, t). \tag{6}$$

Equations (1-3) define ionization degree $Z = n_e/n_p$ (1) and energies of electron (2) and ion (3) subsystems.

Equations (1-3) are solved together with hydrodynamical equations (4-6). Lagrangian variable x^0 is linked to moving substance. The variable x^0 is the initial position of material particle. The x gives direction normal to the irradiated surface. One dimensional approach is valid since radial size of focal spot is large in comparison with attenuation depth $D_{att}(h\nu = 20.2\text{eV}) = 9\text{nm}$ [10].

Equation (1) describes variation of concentration of free electrons n_e in moving material particle x^0 under action of XRL photo-ionization, impact ionization, and recombination. At our time intervals, contributions of photo-recombination and ambipolar diffusion are small. Diffusion is weak as a result of large mass of holes in the narrow valence band. Therefore we neglect diffusion in equation (1) and neglect electron heat conduction in equation (2). Phonon heat conduction is small. Laser flux $I[\text{W/cm}^2]$ defines energy production per unit of volume $\partial I/\partial x = -I/D_{att}$ in equation (2). Volume energy absorption and energy of photon $h\nu$, absorbed at one-photon transition of electron from valence to conduction band, give volume rate of free electron production in ionization equation (1).

Energy flux in (1,2) is

$$I(x^0, t) = \frac{F}{\sqrt{\pi}\tau_L} \exp\left(-\frac{t^2}{\tau_L^2}\right) \exp\left(-\frac{x^0}{D_{att}}\right). \tag{7}$$

In (7) value F [mJ/cm^2] is XRL fluence absorbed by dielectrics. Thickness of the LiF disk is 2 mm, see Section 2. This is a thick layer (2 mm$\gg D_{att} \approx 9$nm) and incident fluence is totally absorbed in a surface layer (no transmission, no reflection). Initially, the absorbing dielectric is placed at the right semiaxis $x > 0$. Time is measured from the maximum of a laser pulse (7). Computer simulation starts from a distant wing of Gaussian function (7) at the instant $t_{start} = -5\tau_L$.

Electron energy E_e in (2) is measured from the bottom of the conduction band. It includes thermal and quantum energy contributions.

Adiabatic expansion works for electron and ion subsystems (2), (3) are $p_e \partial u/\partial x^0$ and $p_i \partial u/\partial x^0$. Gradient of the total pressure $p = p_e + p_i$ governs the change of momentum in dynamical equation (4).

4 Lithium fluoride equation of state, ionization and recombination rates and electron-ion energy exchange

To integrate numerically the system of equations (1)-(6) we need the equation of state (EOS), frequency of impact ionization by free electrons ν_{imp}, recombination coefficient κ_{rec}, and electron-ion energy transfer coefficient α. As for EOS of LiF, we present ionic part of EOS as $E_i(T_i, \rho)$, $p_i(T_i, \rho)$. Electronic excitations are included within

the effective mass approximation. Comparison of EOS for LiF and aluminum (Al) taken from the work [11] shows their close similarity. It makes it possible to use better known wide-range EOS of Al from [11, 12] for computer simulation of LiF, under the action of XRL.

Impact ionization frequency ν_{imp} in equation (1) was the same as in the paper [2] from the work [13]. Three-body recombination coefficient κ_{rec} can then be defined from detailed equilibrium [13].

When the electron concentration in the conduction band of LiF is small, crystal retains its ionic character. In this situation, conduction band electrons interact more extensively with longitudinal optical phonons [14]. Energy transferred from electrons to longitudinal optical phonons per unit volume and unit time can be presented in the form

$$\frac{dE}{dt} = \alpha(T_e - T_i). \tag{8}$$

with electron-phonon coupling factor α

$$\alpha = \sqrt{\frac{2}{\pi}} \frac{k_B n_e}{t_{at}} \sqrt{\frac{m_e}{m} \left(\frac{\varepsilon_{at}}{k_B T_e} \right)^3} \left(\frac{\hbar\omega_0}{\varepsilon_{at}} \right)^2 \int_0^{q_D} \frac{dq}{q} \exp \left(-\frac{\hbar^2 \left(\frac{q}{2} + \frac{m_e \omega_0}{\hbar q} \right)^2}{2 m_e k_B T_e} \right). \tag{9}$$

Here $\varepsilon_{at} = 27.2$ eV is the atomic energy unit, $t_{at} = 2.4 \cdot 10^{-17}$s is the atomic time unit, and q_D is the Debye wave vector. Electron-phonon coupling factor α in (9) is proportional to n_e at small n_e. With n_e increase, an ionic crystal transforms into a configuration similar to a covalent crystal, since the number of F^- ions gradually disappears as number of electrons, lifted from valence band, increases. Therefore, strong electron- optical phonon interaction decreases. This process saturates growth of α.
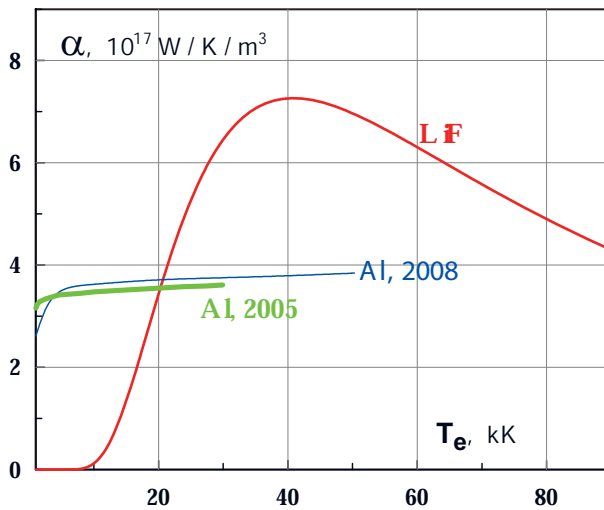

Fig. 4 Comparison of coefficient α for dielectric and metal. There is an obvious difference in α (α gives power transfer per unit of volume) at small temperatures connected with small values of Z in dielectrics. Dependencies for Al are from [15] "Al, 2005" and from [16, 17] "Al, 2008". (Online colour: www.cpp-journal.org).

In Fig. 4 electron-phonon coupling factor α for LiF is shown together with its value for a simple metal such as Al for the comparison. Coefficients α for aluminum, shown as the curves "Al, 2005" [15] in Fig. 4 were calculated taking into account Thomas-Fermi screening of Coulomb interaction without the use of any adjustable parameters. The curve "Al, 2008" in Fig. 4 has been calculated in [16] with the use of approach [18, 19]. It should be mentioned, that very different approaches [15] and [16] give similar results for the coefficient α of Al, see Fig. 4. Calculated values of α for LiF have been used in the computer simulations of system of equations (1-6).

5 Heating and expansion dynamics of LiF crystal under short EUV-FEL pulse

Equations (1-6) with parameters described in Section 4 were used to simulate action of EUV-FEL onto LiF dielectric crystal. Formation and propagation of shock after EUV-FEL action are shown in Figs. 5–7 with parameters typical for experiments (pulse duration $\tau_L = 300$ fs, photon energy 20.2 eV, $D_{att} = 9$ nm).
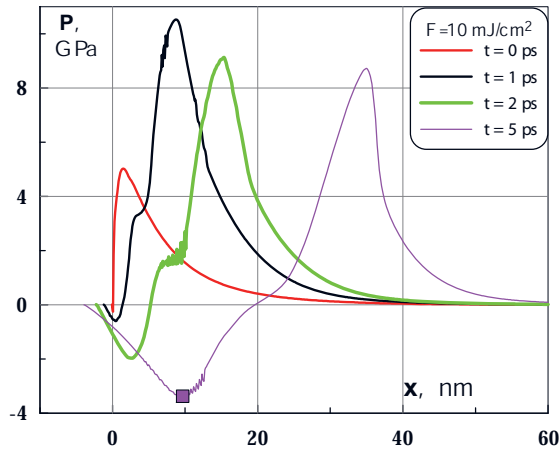
Fig. 5 Formation of compression wave after action of EUV-FEL pulse in the ablation near-threshold regime with $\tau_L = 300$ fs and fluence $F = 10$ mJ/cm^2. The square marker in the pressure profile for $t = 5$ps gives position $(t, x, \text{ or } x^0)$ and absolute value of the maximum instant negative pressure $|p_{neg}(t = 5\text{ps})|_{max}$. (Online colour: www.cpp-journal.org).
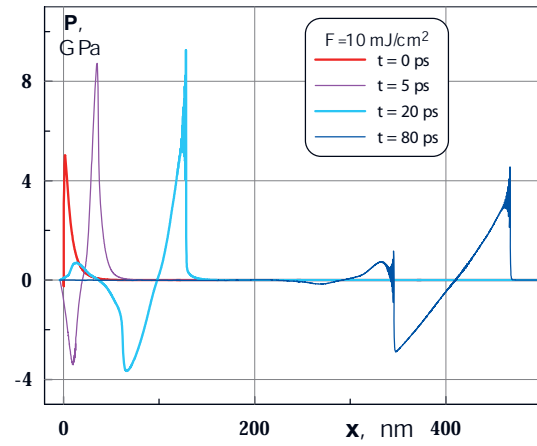
Fig. 6 Appearance of shock as a result of breaking the compression wave $\tau_L = 300$ fs, $F = 10$ mJ/cm^2. Let us mention that two shocks appear: one before the compression wave, while the other behind the stretching wave. There is also appearance of second compression $p > 0$ and second stretching $p < 0$ behind main "plus and minus" acoustic pulse, compared with paper [20]. (Online colour: www.cpp-journal.org).

At instant $t = 0$ half of fluence is delivered, see (7). Maximum of total pressure $p = p_i + p_e$ is achieved slightly later the end of a heating laser pulse. Because, firstly, two-temperature relaxation lasts longer than $\tau_L = 300$ fs, and, secondly, electronic gas is softer than condensed matter (at equal internal energies of electron and ion subsystems pressure p_e is smaller than p_i). After propagation through some distance, the compression wave breaks due to its non-linearity and forms a pressure jump (shock wave). The more non-linear is the wave (larger F, p), the faster it breaks. Shock decays during its subsequent propagation into bulk, see Figs. 6 and 7. Shock attenuation is faster for more non-linear shock. This attenuation is connected with rarefaction wave coming to the shock from the vacuum boundary side.

Near threshold fluence $F_{abl} \approx 10$ mJ/cm^2 the maximum electron temperature is $T_e \approx 20$ kK, the maximum ionization degree is near 3%. Two-temperature relaxation lasts $t_{eq} \sim 1$ps. Maximum T_i is 1.5 kK. The values for fluence $F = 180$ mJ/cm^2 are: $T_e|_{max} \approx 110$kK, $Z|_{max} \approx 0.4 - 0.5$ (in the dense part of LiF where $\rho \approx 2.6$ g/cc near the end of two-temperature relaxation), $T_i|_{max} \approx 10$kK, $t_{eq} \approx 1 - 2$ps. Fluence $F \approx 180$ mJ/cm^2 is the highest fluence achieved in EUV-FEL experiments presented in Section 2.

Low fluence $F \sim F_{abl}$ and high fluence $F \sim 200$mJ/cm^2 EUV-FEL pulses produce different negative pressure profiles which are responsible for spallative ablation at low fluence. Spallative mechanism of ablation has been proposed for explanation of very low values of ablation threshold in case of XRL [2]. In work [2] only the near-threshold case for Ag XRL has been considered experimentally and theoretically. Here we study ablation in wide range of EUV-FEL fluencies.

From Figs. 5–8 we see that in the near-threshold case, negative pressure is achieved in early stages, at shallow depth ≈ 10 nm, and its amplitude $|p_{neg}| \approx 3.5$ GPa is approximately half of the amplitude of compression wave. At large fluencies, the situation is different. Negative pressures appear later, and at significant depths, their maximum amplitude $|p_{neg}|_{max}$ is of the same order as in the near-threshold case. But now, this amplitude is negligible part (less then 0.1 for $F = 180$ mJ/cm^2) of the maximum compression pressure.

The dependencies $|p_{neg}|_{max}(x^0)$ in Fig. 8 show how the maximum tensile stress $|p_{neg}|_{max}$ evolves in space and time as the pressure waves presented in Figs.5–7 penetrate into the LiF target. The square markers in Figs. 5 and 8 help to understand the sense of dependencies in Fig. 8. As was stated in Section 4, we use EOS of Al [11, 12] in computer simulation. In this case, the maximum cold negative pressure $p_{neg}|_{max}(T = 0)$ is ≈ 12 GPa according to paper [20] and its References. In simulations (Figs. 5-8) we did not use technique which allows to include kinetics of nucleation (this will need another paper). In this case fragmentation is achieved

when the system touches the spinodal. Simulations show that in our calculations, presented in 5-8, in cold part of our target the value of tensile stress near $p_{neg}|_{max}(T = 0)$ for Al is not achievable in the range of considered fluencies. Therefore, we did not see separation of a somewhat cold spallation plate from the rest of a target as it was in the paper [20]. But we see evaporation and fragmentation of a rather hot matter from a thin surface layer when fluence F is large. This means, that in our simulations, the system touches the hot part of the spinodal (the spinodal ends in the critical point) and can not achieve the cold part of the spinodal which ends in the point $p_{neg}|_{max}(T = 0)$.
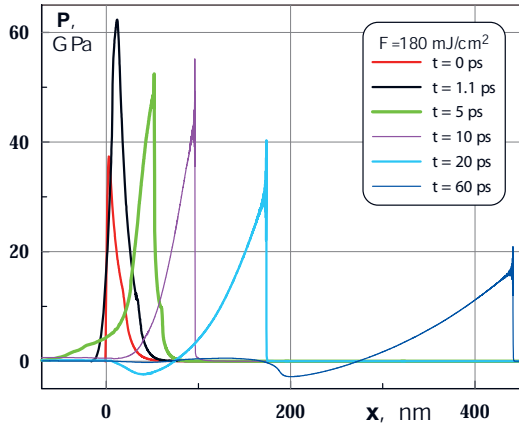

Fig. 7 Formation of powerful acoustic disturbance after action of strong EUV-FEL pulse, $\tau_L = 300$ fs, $F = 180$ mJ/cm^2.
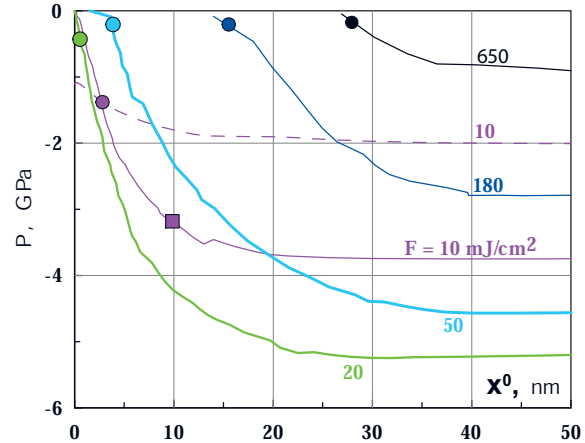(Online colour: www.cpp-journal.org).

Fig. 8 The continuous curves give dependencies $|p_{neg}|_{max}$ on Lagrangian coordinate x^0. The square marker in profile $F = 10$mJ/cm^2 corresponds to the apex point of the well in Fig. 5 marked by the same marker. Its coordinates are: $t = 5$ps, $|p_{neg}|_{max} = 3.4$ GPa, $x = 10$ nm, $x^0 = 9.7$ nm. The difference between x and x^0 is due to motion of substance. The dashed curve presents material strength p_{lim} for the case $F = 10$ mJ/cm^2. Fluencies are written as digits near the curves.
(Online colour: www.cpp-journal.org).

To estimate thickness of the cold spallation plate, we found the material strength $p_{lim}(T)$ and compared it with values of $|p_{neg}|_{max}(x^0)$ in simulations. The dashed curve in Fig. 8 gives the profile of material strength $p_{lim}(x^0)$ in substance heated by EUV-FEL pulse. Dependence $p_{lim}(T)$ has been taken as 30%-60% value of material strength for Al obtained from the paper [21]. In Fig. 8, the intermediate dependence $p_{lim}(T)[\text{GPa}] = -2.2 + 0.7T[\text{kK}]$ is shown as the dashed curve. A temperature profile $T(x)$, taken from simulation has been substituted into the function $p_{lim}[T(x^0)]$. The intersection point of the curves $p_{lim}(x^0)$ and $|p_{neg}|_{max}(x^0)$ is denoted by the circle marker in Fig. 8 for the case with $F = 10$ mJ/cm^2. Intersections at the different fluencies F are denoted by the different circle markers. Simulations demonstrate slow growth of the crater depth with increasing of fluence.

6 Conclusion

Warm dense matter, arising under the action of ultrashort EUV-FEL pulse onto LiF dielectric crystal, is characterized by high temperature of conduction electrons, with their number density achieving values of the order of atom number density at maximum laser fluences in our experiments. Expansion of matter, heated and pressurized through the electron-ion energy exchange, gives rise to the spallative ablation at small fluences and gaseous outflow from a target in the case of large fluences. Ablation threshold is low in comparison with a longer nanosecond XRL.

References

[1] A.Ya. Faenov, N.A. Inogamov, V.V. Zhakhovskii, V.A. Khokhlov, K. Nishihara, Y. Kato, M. Tanaka, T.A. Pikuz, M. Kishimoto, M. Ishino, M. Nishikino, T. Nakamura, Y. Fukuda, S.V. Bulanov, and T. Kawachi, Applied Physics Letters **94**, 231107 (2009).

[2] N.A. Inogamov, A.Ya. Faenov, V.A. Khokhlov, V.V. Zhakhovskii, Yu.V. Petrov, I.Yu. Skobelev, K. Nishihara, Y. Kato, M. Tanaka, T.A. Pikuz, M. Kishimoto, M. Ishino, M. Nishikino, Y. Fukuda, S.V. Bulanov, T. Kawachi, S.I. Anisimov, and V.E. Fortov, Contrib. Plasma Phys. **49**, 455 (2009).

[3] T. Inagaki, S. Imoue, M. Ishi, Y. Kim, H. Kimura, M. Kitamura, T. Kobayashi, H. Maesaka, T. Masuda, S. Matsui, T. Matsushita, X. Marechal, M. Nagasono, H. Ohashi, T. Ohata, T. Ohshima, K. Onoe, K. Shirasawa, T. Takagi, S. Takahashi, M. Takeuchi, K. Tamasaku, R. Tanaka, Y. Tanaka, T. Tanikawa, T. Togashi, S. Wu, A. Yamashita, K. Yanagida, C. Zhang, H. Kitamura, and T. Ishikawa, Nature Photonics **2**, 555 (2008).

[4] T. Shintake, H. Tanaka, T. Hara, T. Tanaka, K. Togawa, M. Yabashi, Y. Otake, Y. Asano, T. Fukui, T. Hasegawa, A. Higashiya, N. Hosoda, T. Inagaki, S. Inoue, Y. Kim, M. Kitamura, N. Kumagai, H. Maesaka, S. Matsui, M. Nagasono, T. Ohshima, T. Sakurai, K. Tamasaku, Y. Tanaka, T. Tanikawa, T. Togashi, S. Wu, H. Kitamura, T. Ishikawa, T. Asaka, T. Bizen, S. Goto, T. Hirono, M. Ishii, H. Kimura, T. Kobayashi, T. Masuda, T. Matsushita, X. Marechal, H. Ohashi, T. Ohata, K. Shirasawa, T. Takagi, S. Takahashi, M. Takeuchi, R. Tanaka, A. Yamashita, K. Yanagida, and C. Zhang, Physical Review Special Topics - Accelerators and Beams **12**, 070701 (2009).

[5] M. Kato, N. Saito, T. Tanaka, Y. Morishita, H. Kimura, H. Ohashi, M. Nagasono, M. Yabashi, K. Tono, T. Togashi, A. Higashiya, and T. Ishikawa, Nuclear Instruments and Methods in Physics Research A **612**, 209 (2009).

[6] G. Baldacchini, S. Bollanti, F. Bonfigli, P.Di Lazzaro, A.Ya. Faenov, F. Flora, T. Marolo, R. M. Montereali, D. Murra, E. Nichelatti, T. Pikuz, A. Reale, L. Reale, A. Ritucci, and G. Tomassetti, IEEE Journal of Selected Topics in Quantum Electronics **10**, 1435 (2004).

[7] G. Baldacchini, S. Bollanti, F. Bonfigli, F. Flora, P.Di Lazzaro, A. Lai, T. Marolo, R. M. Montereali, D. Murra, A. Faenov, T. Pikuz, E. Nichelatti, G. Tomassetti, A. Reale, L. Reale, A. Ritucci, T. Limongi, L. Palladino, M. Francucci, S. Martellucci, and G. Petrocelli, Rev. Sci. Instrum. **76**, 113104 (2005).

[8] G. Tomassetti, A. Ritucci, A. Reale, L. Palladino, L. Reale, L. Arrizza, G. Baldacchini, F. Bonfigli, F. Flora, L. Mezi, R. M. Montereali, S.V. Kukhlevsky, A. Faenov, T. Pikuz, and J. Kaiser, Europhys. Lett. **63**, 681 (2003).

[9] A.Ya. Faenov, Y. Kato, M. Tanaka, T.A. Pikuz, M. Kishimoto, M. Ishino, M. Nishikino, Y. Fukuda, S.V. Bulanov, and T. Kawachi, Optics Letters **34**, 941 (2009).

[10] E.D.Palik (Ed.), ”Handbook of Optical Constants of Solids“, Academic Press, New York, 1998.

[11] Shock wave database: http://teos.ficp.ac.ru/rusbank/.

[12] A.V. Bushman, G.I. Kanel’, A.L. Ni, and V.E. Fortov, ”Intense dynamic loading of condensed matter“, Taylor & Francis, 1993.

[13] I.I. Sobelman, L.A. Vainshtein, and E.A. Yukov, ”Excitation of Atoms and Broadening of Spectral Lines“, Springer Series on Atoms and Plasma. Springer, 2007.

[14] A.I. Anselm, ”Introduction to Semiconductor Theory“, Prentice-Hall, Englewood Cliffs, NJ, 1981.

[15] Yu.V. Petrov, Laser and Particle Beams **23**, 283-289 (2005).

[16] Z. Lin, L.V. Zhigilei, and V. Cell, Phys. Rev. B **77**, 075133 (2008).

[17] http://www.faculty.virginia.edu/CompMat/electron-phonon-coupling/.

[18] P.B. Allen, Phys. Rev. Lett. **59**, 1460 (1987).

[19] X.Y. Wang, D.M. Riffe, Y.S. Lee, and M.C. Downer, Phys. Rev. B **50**, 8016 (1994).

[20] V.V. Zhakhovskii, N.A. Inogamov, Yu.V. Petrov, S.I. Ashitkov, and K. Nishihara, Applied Surface Science **255**, 9592 (2009).

[21] M.B. Agranat, S.I. Anisimov, S.I. Ashitkov, V.V. Zhakhovskii, N.A. Inogamov, P.S. Komarov, A.V. Ovchinnikov, V.E. Fortov, V.A. Khokhlov, and V.V. Shepelev, JETP Letters **91**, 471-477 (2010).